Dual functionalized interstitial N atoms in Co3Mo3N enabling CO2 activation

Journal:	*ACS Catalysis*
Manuscript ID	cs-2022-005838.R2
Manuscript Type:	Article
Date Submitted by the Author:	23-Mar-2022
Complete List of Authors:	Feng, Kai; Tsinghua University, Department of Chemical Engineering Tian, Jiaming; Tsinghua University, Department of Chemical Engineering Zhang, Jiajun; Tsinghua University, Department of Energy and Power Engineering Li, Zhengwen; Tsinghua University, Department of chemical engineering Chen, Yuxin; Tsinghua University, chemical engineering Luo, Kai Hong; University College London, Department of Mechanical Engineering Yang, Bin; Tsinghua University, Energy and Power Engineering Yan, Binhang; Tsinghua University, Department of Chemical Engineering

Dual functionalized interstitial N atoms in Co_3Mo_3N enabling CO_2 activation

Kai Feng[1], Jiaming Tian[1], Jiajun Zhang[2], Zhengwen Li[1], Yuxin Chen[1], Kai Hong Luo[3], Bin Yang[2], Binhang Yan[1,*]

[1] *Department of Chemical Engineering, Tsinghua University, Beijing 100084, China*

[2] *Center for Combustion Energy, Key Laboratory for Thermal Science and Power Engineering of Ministry of Education, and International Joint Laboratory on Low Carbon Clean Energy Innovation, Tsinghua University, Beijing 100084, China*

[3] *Department of Mechanical Engineering, University College London, Torrington Place, London WC1E 7JE, UK*

*Corresponding author

Telephone: (86) 010-62797920; Email: binhangyan@tsinghua.edu.cn

KEYWORDS: Reverse water-gas shift; interstitial light element; Co_3Mo_3N; dual functionalized N atoms; CO_2 activation.

ABSTRACT

The introduction of light elements into interstitial sites of metals can significantly modify their surface structure and electronic properties, and thus enhance the catalytic performance. However, it is still unclear how the interstitial light elements promote the catalytic activity. Herein, N atoms are incorporated into the bimetallic CoMo system to synthesize Co_3Mo_3N as a efficient catalyst for reverse water-gas shift (RWGS) reaction. Compared to CoMo, Co_3Mo_3N significantly promotes the catalytic performance, where the removal of O-containing intermediates is identified as the rate-determining step. The enhanced activity is attributed to

the dual functions of interstitial N atoms in Co_3Mo_3N, which provide additional sites for supplying H atoms to facilitate the hydrogenation of O-containing intermediates and accept electrons from Mo to weaken the binding ability of Mo to O-containing intermediates. These dual functionalized interstitial N atoms promote the redox cycle during the RWGS process and thus improve the catalytic performance. Our work provides understandings of the interstitial light elements-promoted catalytic performance relationship.

1. INTRODUCTION

Over the past century, catalysis technologies have revolutionized our production mode and lifestyle, naturally leading to a long-term need for a set of newly-designed catalysts with excellent performance.[1] The Sabatier's principle provides a criterion for designing catalysts, which indicates that a good catalyst should bind the reaction intermediates strongly enough to activate the reactants but weakly enough to allow desorption of products.[2] It also represents a challenge to finely tune the electronic structure of catalysts, because these binding energies are in principle determined completely by the electronic structure of active metals. However, it is difficult to achieve an optimal binding state for key intermediates as the intrinsic electronic structure of active metals cannot be altered freely.[2-7]

The introduction of light elements (H,[8-10] B,[11-13] C,[14-16] N,[17-19] P,[20-23] etc.) into the interstitial site of metals can significantly modify the electronic properties of surface atoms, and thus tune the catalytic performance. Transition metal carbides (carbon atoms are doped into the interstitial sites of the transition metal) are a class of typical catalysts that exhibit enhanced catalytic performance in various catalytic processes due to the unique electronic

structure induced by the incorporation of C.[24-29] For example, it has been demonstrated that α-MoC as a special catalyst or functional support exhibits outperformed performance in catalytic processes related to low-temperature O-H activation, including ultralow temperature water-gas shift reaction,[30] methanol reforming,[31-34] etc. Moreover, the incorporation of light element atoms into the transition metal lattice also leads to changes in the geometric properties of surface atoms and thereafter affects the catalytic performance. Recently, He et al. used the expansion and contraction of Pd nanocubes via the phosphorylation and dephosphorylation process to induce strain in the Pt(100) lattice of the Pd@Pt core-shell structure and elucidated the strain-activity correlation for the methanol oxidation and hydrogen evolution reactions.[20] In addition, it is also found that the light elements in the interstitial site of transition metals could directly participate in reactions and enhance the catalytic performance. Wang et al. found that the N atom in Co_4N catalyst could directly interact with H_2 to form $CoNH_x$ during CO_2 hydrogenation, and the amido-hydrogen atoms would directly interact with CO_2 to form *HCOO species, and thus enhance the yield of methanol.[19] Furthermore, thanks to the development of *in-situ* characterization techniques, it is also demonstrated that the light elements might also be introduced into the metal lattice as a new active center during catalytic processes.[35] The C from the dissociation of CH_4 could be introduced into NiGa to form $Ni_3GaC_{0.25}$ during dry reforming of CH_4, and the interstitial C is involved in the redox cycle of the reaction and thus inhibits the generation of coke.[36]

The reverse water-gas shift (RWGS) reaction, a well-known CO_2 utilization reaction for carbon capture, utilization and storage (CCUS) technologies, is critical to the overall CO_2 hydrogenation performance as it is the initial step of CO_2 hydrogenation and a variety of

subsequent products are derived based on the RWGS+X (e. g., CO hydrogenation) pathway.[35, 37-40] For this process, the introduction of light elements has also been demonstrated to significantly enhance the catalytic performance. It is found that the product selectivity of Ni-based catalysts could be shifted from CH_4 to CO due to the introduction of P.[41, 42] Moreover, the Mo_2C and Fe_2C_5 catalysts are also used in the RWGS reaction and show excellent catalytic performance.[15, 43] However, the origin of the interstitial light elements-promoted RWGS process still remains unclear. It also encourages us to further explore the changes in structure-activity relationships due to the introduction of interstitial light elements and thus obtain the fundamental understanding for the RWGS process.

Herein, to accelerate the redox cycle during the RWGS reaction, the light element N is introduced to CoMo to fine-tune its electronic structure and provide more sites for supplying active H atoms during reaction. Firstly, N atoms were successfully introduced into bimetallic CoMo catalysts to form bimetallic nitride Co_3Mo_3N over a typical nitridation process. A series of structural characterization and temperature-programmed experiments results indicated that the introduced N atoms could provide additional sites for the supply of H species during CO_2 activation, leading to an enhanced RWGS activity. Further experimental results and DFT calculations suggested that the introduced N atoms did not interact with Co, but accepted electrons from Mo and thus induced the formation of the positive charged Mo ($Mo^{\delta+}$), weakening the binding ability of Mo to O-containing intermediates. Both the two functions of the introduced N atoms accelerate the removal of O from the surface by H_2, contribute to the enhanced redox cycle and consequently improve the RWGS activity. This work not only identifies the origin of N-promoted RWGS performance for bimetallic nitride but also provides

new insights into the understanding of the structure-performance relationship.

2. EXPERIMENTAL SECTION

2.1. Catalyst preparation

$CoMoO_4$ was synthesized by a hydrothermal method. Typically, 14 mmol $Co(NO_3)_2 \cdot 6H_2O$ and 2 mmol $H_{32}Mo_7N_6O_{28}$ were dissolved in 180 mL deionized water. Next, the solution was transferred into a Teflon-lined stainless-steel autoclave and then placed in an oven at 160 ℃ for 6 h. The product was centrifuged and washed with deionized water, and then dried at 100 ℃ overnight. Finally, the dried powder was calcined at 450 ℃ in air for 4 h in a muffle furnace. The final product obtained is $CoMoO_4$, denoted as CMO.

Co_3Mo_3N (CMN) and CoMo (CM) were synthesized through the reduction of CMO in different atmospheres. For the synthesis of CMN, the as-obtained CMO was annealed at 850 ℃ with a heating rate of 10 ℃/min in a N_2/H_2 flow (5 mL/min N_2 with 15 mL/min H_2) for 1 h. CM was obtained through a similar treatment in an Ar/H_2 flow. Notably, after cooling in a reduction atmosphere, a CO_2/Ar mixture (5 mL/min CO_2 and 15 mL/min Ar) is necessary for the passivation of CMN and CM at room temperature.

SiO_2-supported Co catalysts were synthesized by the impregnation method for comparison. Typically, 1 g commercial SiO_2 (Alfa Aesar) was mixed with an aqueous solution of $Co(NO_3)_2$ (9.94 mmol, 36.94 wt%). After evaporating the water at 80 ℃, the powders were collected and annealed at 450 ℃ for 4 h in a muffle furnace. Then, the as-annealed samples were reduced in an Ar/H_2 flow (5 mL/min Ar with 15 mL/min H_2) at 600 ℃ for 1 h in a tube furnace and the sample was denoted as Co/SiO_2.

2.2 Structural characterization

Samples for transmission electron microscopy (TEM) were dropcasted onto carbon-coated copper grids from H_2O suspensions. TEM and energy dispersive X-ray spectroscopy (EDX) elements mapping images were obtained with a FEI Talos F200X TEM operating at 200 kV. X-ray photoelectron spectroscopy (XPS) data were collected on a PHI Quantera II instrument from Ulvac-Phi Inc. using monochromatic Al Kα radiation (λ = 0.8339 Å). The binding energies for all spectra were corrected to the C 1s peak at 284.8 eV. The surface area of catalysts was evaluated through BET analysis using a Quantachrome Autosorb-iQ2-C. X-ray absorption spectroscopy was performed at beamline 4B9A of the Beijing Synchrotron Radiation Facility (BSRF). The powder samples were coated onto the 3 M tapes examined in a transmission mode, and the data were collected from 7516 eV to 8519 eV. Data processing of XANES and EXAFS was carried out using the Athena software package.

2.3 Catalytic performance evaluation

CO_2 hydrogenation experiments were carried out using a flow reactor under atmospheric pressure. Firstly, 30 mg catalyst was loaded into a quartz tube with an inner diameter of 4 mm and held in place by quartz wool. Before each CO_2 hydrogenation experiment, the catalyst was reduced in a 5 mL/min N_2 or Ar with 15 mL/min H_2 flow (N_2 for CMN and Ar for CM) at 600 ℃ for 1 h to remove the surface passivation layer. Next, the reactor was cooled down to 400 ℃ in an Ar flow (30 mL/min), and then the inlet flow was switched to the reactants (i.e., 10 mL/min CO_2, 10 mL/min H_2, and 20 mL/min Ar) for CO_2 hydrogenation.

Furthermore, the step temperature CO_2 hydrogenation test from 300 to 400 ℃ was also performed under the same experimental conditions, in which the reaction time for each

temperature step is 80 min. According to the Arrhenius equation, the activation energy (E_a) of CMN and CM catalysts for the RWGS reaction was also obtained. Notably, to reduce the impact of catalyst deactivation on E_a evaluation, the stepwise cooling and heating treatments (400-300-400 ℃) were evaluated using the method suggested in the literature (**Figure S1**).[44]

The gas chromatograph (Agilent 7890B) equipped with a flammable ionization detector (FID) and a thermal conductive detector (TCD) was used to analyze the concentration of gas products. The response factor of each reactant and product was calibrated using standard curve methods. The conversion of CO_2 (X_{CO_2}) is defined as:

$$X_{CO_2} = \frac{F_{CO(outlet)} + F_{CH_4(outlet)}}{F_{CO_2(inlet)}} = \frac{C_{CO(outlet)} + C_{CH_4(outlet)}}{C_{CO_2(inlet)}} \quad (1)$$

The selectivity of CO (S_{CO}) is defined as:

$$S_{CO} = \frac{F_{CO(outlet)}}{F_{CO(outlet)} + F_{CH_4(outlet)}} = \frac{C_{CO(outlet)}}{C_{CO(outlet)} + C_{CH_4(outlet)}} \quad (2)$$

The carbon balance was calculated according to the following equation:

$$\text{Carbon balance} = \frac{C_{CO(outlet)} + C_{CO_2(outlet)} + C_{CH_4(outlet)}}{C_{CO_2(inlet)}} \quad (3)$$

where F is the flow rate of reactants or products (mol/min), C is the concentration of reactants or products (%). All catalytic performance data were calculated by averaging data points in cooling and heating sections at the same reaction temperature.

2.4 Temperature-programmed experiments

CO_2 hydrogenation temperature-programmed surface reaction (TPSR), CO_2 temperature-programmed oxide (TPO), and temperature-programmed H/D (TP-H/D) exchange experiments were carried out in a flow reactor. 20 mg catalyst was loaded into a quartz tube with an inner

diameter of 4 mm. Before each experiment, the catalyst was reduced in a 5 mL/min N_2 or Ar with 15 mL/min H_2 flow (N_2 for CMN and Ar for CM) at 600 ℃ for 1 h to remove the surface passivation layer. Next, the reactor was cooled down to room temperature in an Ar flow (30 mL/min), and then the inlet flow was switched to the reaction gas (CO_2: H_2: Ar = 10: 10: 20 mL/min for CO_2 hydrogenation TPSR; CO_2: Ar = 10: 10 mL/min for CO_2 TPO; D_2: H_2: Ar = 2: 2: 16 mL/min for TP-H/D exchange) and the reactor was heated to 600 ℃ with a heating rate of 10 ℃/min. The gas products were detected online using an FTIR spectrometer (Thermo Nicolet iS50).

H_2 temperature-programmed reduction (H_2-TPR) of CM and CMN catalysts after CO_2 hydrogenation for 1 h was carried out in a flow reactor. 20 mg catalyst was loaded into a quartz tube to perform the CO_2 hydrogenation reaction for 1 h. After cooling down to room temperature, the inlet flow was switched to a 20 mL/min 10 vol% H_2/Ar flow and the reactor was heated to 800 ℃ with a heating rate of 10 ℃/min. The H_2 consumption was detected online using a TCD (Agilent 8860).

2.5 Transient response experiments

CO_2 activation transient response experiments were performed in a flow reactor. 50 mg catalyst was loaded into a quartz tube with an inner diameter of 4 mm. Before transient response experiments, the catalyst was reduced in a 5 mL/min N_2 or Ar with 15 mL/min H_2 flow (N_2 for CMN and Ar for CM) at 600 ℃ for 1 h to remove the surface passivation layer. Next, the reactor was cooled down to 400 ℃, and then the inlet flow was switched to an Ar/H_2 flow (10 mL/min Ar and 10 mL/min H_2) and maintained for 10 min. Finally, the inlet flow was switched to an Ar/CO_2 flow (10 mL/min Ar and 10 mL/min CO_2). The gas products were detected online

using an FTIR spectrometer (Thermo Nicolet iS50).

2.6 In-situ characterization

In-situ X-ray diffraction (XRD) patterns were recorded on a Bruker D8 Advance diffractometer equipped with an Anton Paar XRK-900 furnace operating at 40 kV with CuKα radiation (λ = 1.5406 Å) within the range of 22.5-52.5° with a scanning rate of 0.85°/min. The CMO was exposed to a N_2/H_2 flow (5 mL/min N_2 with 15 mL/min H_2) for reduction. After the first XRD collection at room temperature, the temperature was sequentially increased to 100 ℃, 200 ℃ and 300 ℃ with a ramp of 5 °C/min for XRD measurements. Then, the XRD collection was performed every 10 °C from 300 ℃ to 850 ℃.

Quasi-in-situ Raman spectra were obtained using a laser Raman spectrometer with the exciting line at 325 nm (Horiba LabRAM HR Evolution). 10 mg catalyst was loaded into a quartz tube with an inner diameter of 4 mm. Notably, as shown in **Figure S2**, a plane on the quartz tube was constructed to reduce laser scattering. After the first Raman spectra collection at room temperature, the catalyst was exposed to a 5 mL/min N_2 or Ar with 15 mL/min H_2 flow (N_2 for CMN and Ar for CM) and reduced at 600 °C for 1h. The reduced catalyst was sealed in the quartz tube under N_2/Ar+H_2 atmosphere to collect Raman spectra at room temperature. Next, the same catalyst in the quartz tube was treated sequentially under CO_2 hydrogenation atmosphere for 1 h and 10 h, and then the spent catalysts were sealed in the quartz tube under CO_2+H_2+Ar atmosphere to collect Raman spectra at room temperature.

2.7 Computational Methods

Density functional theory (DFT) calculations were performed using the Vienna ab initio simulation (VASP) package. The frozen-core all-electron projector augmented wave (PAW)

method was used to describe the electron-ion interaction, in which the generalized gradient approximation with the Perdew-Burke-Ernzerhof (PBE) functional was used to simulate the exchange-correlation energy. During the calculation, an energy cutoff of 450 eV was used. The (001) surface of rhombohedral Co_7Mo_6 structure and (111) surface of cubic Co_3Mo_3N structure were modeled with a 2 × 2 slab for CM and CMN catalysts, respectively, in which the top two layers of atoms and the coordination H and O were relaxed. [4, 45-47] In the relaxation, the force convergence criterion was set to 0.03 eV/Å, and the energy convergence criterion was 10^{-4} eV. The crystal orbital Hamilton population (COHP) method was used to analyze the strength of chemical bonds based on the LOBSTER package. Binding energy was also calculated using the following equation:

$$\text{Binding energy} = E_{\text{total}} - E_{\text{slab}} - E_{\text{adsorbate}} \quad (4)$$

where E_{total} is the total energy of adsorbate and catalyst surface, E_{slab} is the total energy of catalyst surface, $E_{\text{adsorbate}}$ is the total energy of adsorbate.

3. RESULTS AND DISCUSSION

3.1 Catalyst synthesis and characterization

Co_3Mo_3N catalysts, denoted as CMN, were synthesized by the nitridation of $CoMoO_4$ (CMO) under N_2/H_2 atmosphere. The CMO precursor was first prepared using a hydrothermal method followed by a post-annealing treatment, then the *in-situ* X-ray diffraction (XRD) experiment was executed to monitor the phase structure evolution from CMO to CMN during the nitridation process. The as-prepared CMO shows a rod-shaped morphology with a diameter of ~1 μm (**Figure S3**) and a pure monoclinic phase structure (PDF-#21-0868). As shown in **Figure 1a** and **Figure S4**, CMO remains stable at low temperature but is reduced to $Co_2Mo_3O_8$

(PDF-#89-7093) and CoO (PDF-#70-2855) when the temperature exceeds 400 ℃. As the nitridation temperature is further increased to 500 ℃, the peak of metallic Co near 44.2° is found while no N-containing species are identified, suggesting that N_2 cannot be effectively dissociated at this time. Above 600 ℃, O atoms in the sample could be thoroughly removed by interacting with H_2 and N atoms begin to be introduced into the sample, in which only the diffraction peaks of Co_3Mo (PDF-#29-0488) and Mo_2N (PDF-#75-1150) are found in the XRD patterns. Further elevating temperature to 680 ℃, the target Co_3Mo_3N (PDF-#89-7953) phase with a small fraction of Co_2Mo_3N (PDF-#04-010-6426) appears. Until 810 ℃, the diffraction peaks of Co_2Mo_3N disappear and a pure Co_3Mo_3N phase is finally obtained, which is consistent with previous reports.[48, 49] TEM images show that the as-obtained CMN preserves the rod shape but becomes porous, exhibiting a Brunner-Emmet-Teller (BET) surface area of ~6 m^2/g (**Figure 1b**). Notably, the high-resolution transmission electron microscopy (HRTEM) image shows a thin oxide layer on the surface of CMN, which is formed during the passivation after the nitridation process (**Figure 1c**). This passivation treatment is necessary to prevent the excessive oxidation of CMN when exposed to air as CMN is highly reactive.[30, 50] Moreover, the energy dispersive X-ray spectroscopy (EDX) elemental mapping results reveal the homogeneous distribution of Co, Mo, and N in Co_3Mo_3N nanorods (**Figure 1d-g**). Therefore, through the nitridation treatment under N_2/H_2 atmosphere, N atoms can be successfully introduced into CoMo bimetallic system to form a cubic Co_3Mo_3N phase.

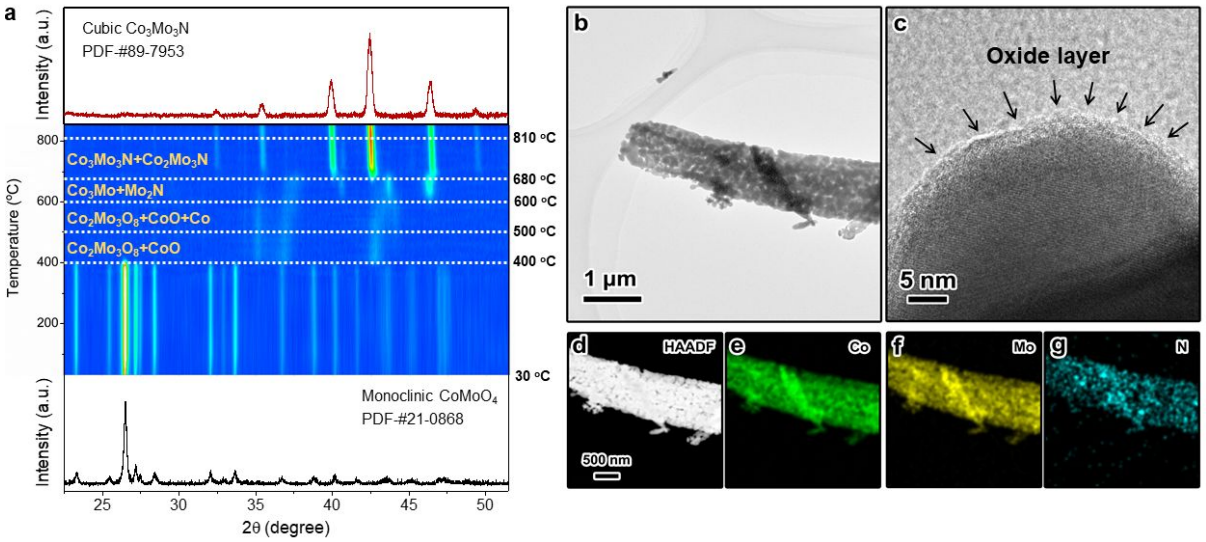

Figure 1 (a) *In-situ* XRD patterns during the nitridation process of $CoMoO_4$ to Co_3Mo_3N. (b) TEM image, (c) high-solution TEM image, and (d)-(g) EDX elemental mapping images of Co_3Mo_3N.

3.2 Catalytic performance evaluation

To understand the effect of introduced N atoms on CO_2 hydrogenation performance, CM was prepared as a control sample through a similar synthesis process under Ar/H_2 atmosphere instead of N_2/H_2 atmosphere. As shown in **Figure S5**, the as-prepared CM shows a mixed phase of a large fraction of Co_7Mo_6 alloy (PDF-#29-0489) and a small fraction of metallic Mo (PDF-#42-1120). Moreover, CM also shows a similar porous rod morphology, surface oxide layer, and BET surface area (~5 m^2/g) to CMN (**Figure S6**). **Figure 2a** and **Table S1** show the steady-state catalytic performance of CM and CMN for CO_2 hydrogenation at 400 ℃ with a space velocity (SV) of 80000 $ml \cdot h^{-1} \cdot g^{-1}$. It is found that both catalysts exhibit ~100% selectivity towards the RWGS reaction while CMN (~8.8%) shows a higher CO_2 conversion than CM (~5.6%). CO_2 hydrogenation experiments over CM and CMN at various temperatures (300-400 ℃) were also carried out. As shown in **Figure 2b**, the CO_2 conversion for both the two catalysts increases with increasing temperature, while the product selectivity is almost

unchanged. CM shows a similar CO_2 conversion at low temperatures, while the CO_2 conversion of CMN obviously exceeds that of CM with elevating the reaction temperature. Moreover, the CO space-time yield (STY) normalized based on metal compositions also reveals that CMN exhibits higher activity than CM, the higher the temperature, the greater the difference (**Figure S7**). This means that CMN is with a higher apparent activation energy (E_a) for the RWGS reaction and thereafter shows better catalytic performance at high temperatures (**Figure 2c**). Therefore, it could be safely concluded that the introduced N atoms into CoMo bimetallic system could effectively enhance its RWGS activity. The over 30 h steady-state flow reaction results also indicate that this enhanced effect caused by introducing N atoms is stable during CO_2 hydrogenation (**Figure 2d**), suggesting that CMN could be a potential catalyst for the RWGS reaction. Notably, a short induction period is observed in the early stages of the stability test for the CMN catalyst, which might be attributed to the depletion of adsorbed active H species from well-known NH_x species in the pretreatment process.[19]

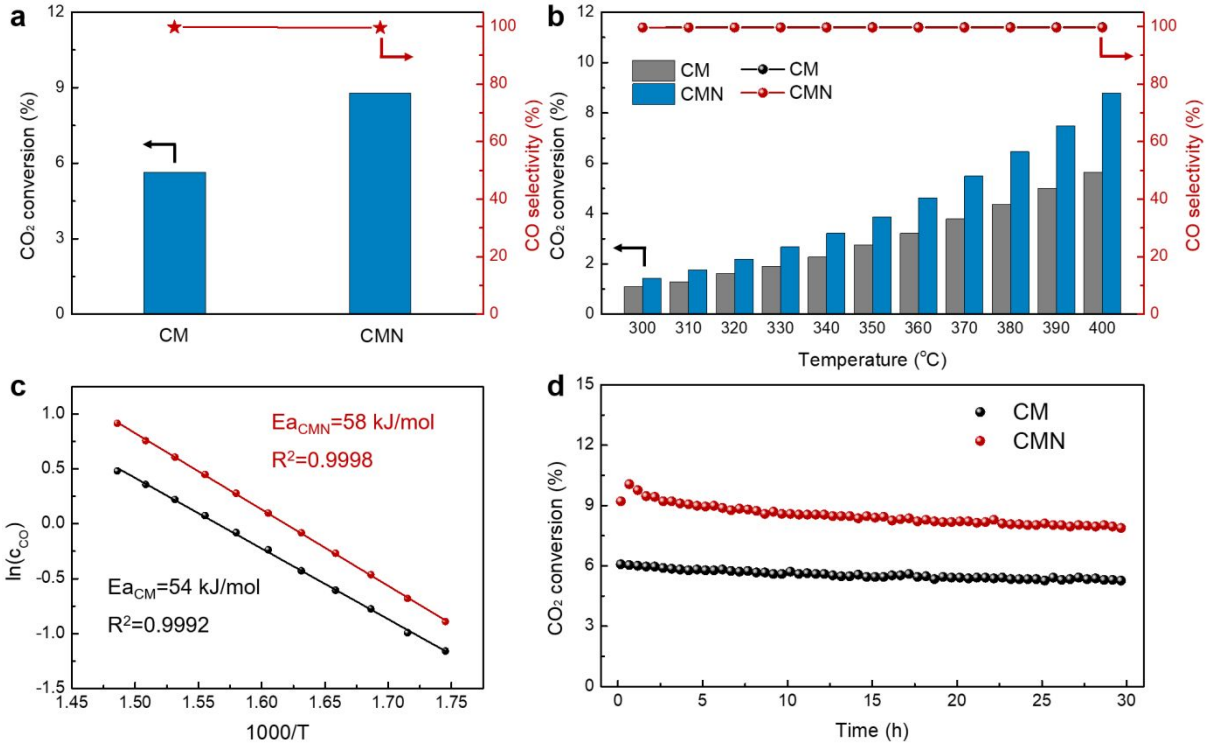

Figure 2 CO_2 conversion and product selectivity of different catalysts for CO_2 hydrogenation at (a) 400 ℃ and (b) temperatures from 300 to 400 ℃. (c) Arrhenius plots and (d) catalytic performance in the long-term stability test at 400 ℃. (30 mg catalyst, $CO_2/H_2/Ar$ = 10/10/20 mL/min for all tests).

3.3 Electronic structure characterization

It is well known that the catalytic performance of a catalyst is in principle determined by its electronic structure.[2] Here, to unravel the origin of the enhanced RWGS activity for CMN, X-ray photoelectron spectroscopy (XPS) and X-ray absorption spectroscopy (XAS) experiments were performed to investigate the electronic structure of CM and CMN. **Figure 3a** shows the XPS spectra of Co 2p region for both catalysts, in which the XPS peaks at 777.8 eV, 780.8 eV, 792.8 eV and 796.9 eV are assigned to Co^0 $2p_{3/2}$, $Co^{\delta+}$ $2p_{3/2}$, Co^0 $2p_{1/2}$ and $Co^{\delta+}$ $2p_{1/2}$, respectively (**Table S2**). It is found that the peak positions corresponding to Co^0 and $Co^{\delta+}$ remain consistent for both catalysts, indicating the electronic structure of Co is not significantly affected by the introduction of N atoms. In contrast, the peak positions corresponding to Mo^0 $3d_{5/2}$, $Mo^{\delta+}$ $3d_{5/2}$, and Mo^0 $3d_{3/2}$ for CMN slightly shift to higher binding energy, implying that there is an electron transfer from Mo to N and the positive charged Mo ($Mo^{\delta+}$) is formed (**Figure 3b and Table S2**). This could be explained by the coordination geometry of N atoms in CMN. According to the standard crystal structure of CMN, the N atom is only coordinated to the Mo atom rather than the Co atom, thus it only accepts the electron from Mo but Co. The N-Mo coordination is also observed at the binding energy of 398.9 eV in the N 1s region for the CMN catalyst (**Figure 3c**). Furthermore, the electronic and fine structure of Co atoms in CM and CMN were further revealed through the Co K-edge XAFS spectra. As shown in **Figure 3d**, both the Co K-edge X-ray absorption near-edge structure (XANES) spectra of CM and

CMN show the weak white-line intensity and similar absorption edge position to Co foil, suggesting that the Co species in CM and CMN exist in metallic state. Further comparisons with the XANES spectra of Co foil, CoO, and Co_2O_3 also confirm that Co in CM and CMN is almost in zero valence state (**Figure 3e**). These results demonstrate that the introduction of N atoms does not change the valence state of Co, which is consistent with the XPS results. However, there are still distinct differences in Co K-edge features between CM, CMN, and Co foil, implying the difference in the coordination geometry of Co atoms in the three samples, which is also demonstrated by the EXAFS results (**Figure 3d inset**). As shown in **Figure 3f**, a broad peak at 2.07 Å is observed for CM, which originates from the fusion of Co-Co (5) coordination and Co-Mo (7) coordination. In contrast, the EXAFS spectra of CMN show two well-defined peaks at 1.95 Å and 2.53 Å, corresponding to Co-Co (6) and Co-Mo (6) coordination, respectively. Compared to the standard structures, it is found that CM and CMN show a similar Co-Co bond length of 2.38 Å but different Co-Mo bond lengths, indicating that the difference in the coordination geometry of Co atoms in CM and CMN should be attributed to the different coordination numbers and Co-Mo bond lengths. Therefore, it could be reasonably inferred that the introduction of interstitial N atoms mainly tunes the electronic structure of Mo rather than Co, thus enhancing the catalytic performance of CMN.

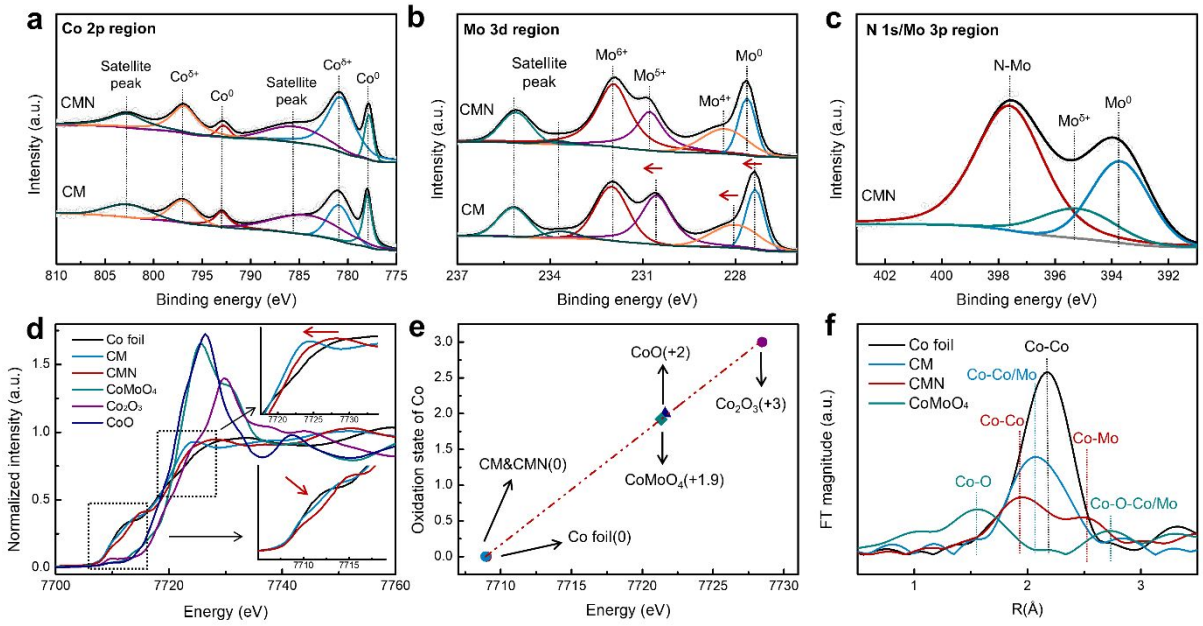

Figure 3 XPS spectra of (a) Co 2p, (b) Mo 3d for CM and CMN and (c) N 1s and Mo 3p regions for CMN. (d) Co K-edge XANES spectra (inset is the zoom of whiteline and pre-edge region), (e) oxidation state of Co and (f) Co K-edge EXAFS spectra of CM, CMN and CMO.

3.4 Rate-determining step identification

To better clarify the origin of the enhanced RWGS catalytic performance due to the introduction of N atoms, it is critical to identify the rate-determining step for both CM and CMN catalysts. As previously reported, the first step for the RWGS reaction is CO_2 activation including direct CO_2 dissociation and H_2-assisted CO_2 dissociation.[39, 51, 52] To identify the CO_2 dissociation pathway, CO_2 temperature-programmed oxidation (TPO) and CO_2 hydrogenation temperature-programmed surface reaction (TPSR) experiments were carried out for CM and CMN catalysts. As shown in **Figure 4a**, the CMN catalyst shows a lower onset temperature (~310 ℃) for direct CO_2 dissociation than CM (~375 ℃) in the absence of H_2, representing a stronger CO_2 dissociation ability for CMN. In comparison, the introduction of H_2 lowers the onset CO_2 dissociation temperature for both catalysts, suggesting that CO_2 is more likely to be

activated with the assistance of H_2 through formate (*HCOO) or carbonyl species (*COOH) during CO_2 hydrogenation (**Figure 4b**). Moreover, it is noteworthy that the CMN catalyst with a stronger direct CO_2 dissociation ability exhibits a lower onset temperature for H_2-assisted CO_2 dissociation than that of the CM catalyst (~180 ℃ for CM and ~207 ℃ for CMN), implying that the introduction of H_2 greatly enhances the CO_2 dissociation ability of CM (even better than CMN). However, these results bring a contradiction that the CM catalyst with a stronger H_2-assisted CO_2 dissociation ability but shows a poorer RWGS activity at high temperatures. To explain this contradiction, the H_2 activation ability of both CM and CMN catalysts was evaluated by temperature-programmed H/D (TP-H/D) exchange experiments. As shown in **Figures 4c** and **4d**, compared to CM (171 ℃), CMN shows a lower onset temperature (135 ℃) for the consumption of H_2 and D_2, which suggests that the incorporation of N atoms significantly enhances the H_2 dissociation ability. Notably, it is also observed that CMN shows a higher onset temperature (280 ℃) for the production of HD than CM (215 ℃), implying that the dissociated H species interact more strongly with CMN. As reported in the previous literature, this might be attributed to the formation of amido groups (NH_x).[19] The formation of NH_x species on CMN is further confirmed by a transient response experiment. As shown in **Figure 4e**, after switching the gas from Ar/H_2 mixture to Ar/CO_2 at 400 ℃ (i.e., the reaction temperature), a small amount of ammonia (NH_3) is detected, providing direct evidence for the existence of NH_x species on CMN. Therefore, it could be inferred that the higher desorption barrier of active H species on CMN makes it more difficult for providing active H atoms to participate in the H_2-assisted CO_2 activation process, and consequently exhibits a lower RWGS activity compared to CM in low-temperature conditions (**Figure 2b** and **Figure 4b**). However,

at high temperatures (e.g., 400 ℃), the dissociation of H_2 and desorption of active H species are easier for both CM and CMN catalysts, thus the additional NH_x species in CMN could provide more active H atoms to participate in the reaction, improving its RWGS activity. The results of transient response experiments also indicate that H_2O and CO could be detected for both CM and CMN with pre-adsorbed hydrogen after switching gas from Ar/H_2 to Ar/CO_2 at 400 ℃, suggesting that the active H species adsorbed on the surface could participate in the RWGS reaction in time. Meanwhile, it is observed that the CMN catalyst shows a higher yield of H_2O and CO, which directly confirms that the CMN catalyst has more adsorbed H species involved in the RWGS reaction. These results demonstrate that introducing N atoms into CoMo bimetallic catalysts increases the sites to increase the supply of H species during the CO_2 hydrogenation reaction and ultimately improves the catalytic performance.

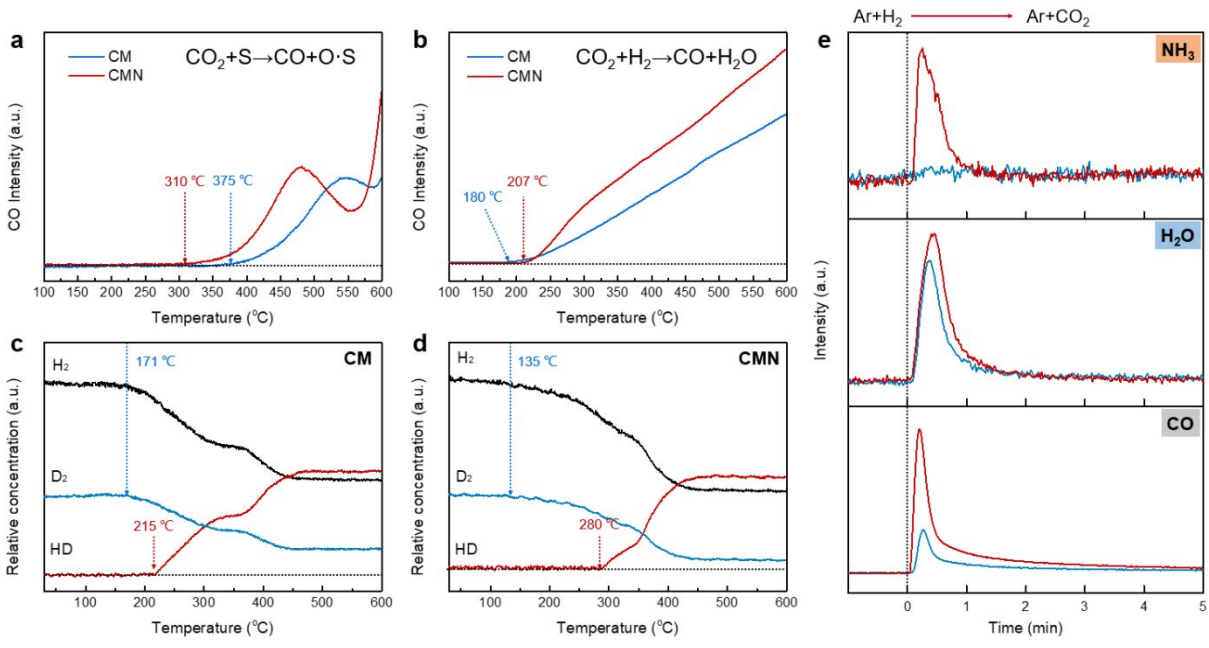

Figure 4 CO signals of (a) CO_2 temperature-programmed oxidation (TPO) and (b) CO_2 hydrogenation temperature-programmed surface reaction (TPSR). Temperature-programmed H/D (TP-H/D) exchange experimental results of (c) CM and (d) CMN. (e) Signal variations of NH_3, H_2O, and CO with time for CM

and CMN catalysts during transient response experiments after switching the reaction gas from Ar/H_2 to Ar/CO_2.

Based on the above results, it is reasonable to speculate that the N-promoted RWGS performance might originate from the enhanced hydrogenation ability of key intermediates instead of CO_2 activation or H_2 dissociation. To this end, H_2 temperature-programmed reduction (H_2-TPR) after CO_2 hydrogenation was performed to evaluate the hydrogenation ability of absorbed species during the reaction. As shown in **Figure 5a**, to exclude the possible effects of exposing catalysts to air, the H_2-TPR test was *in-situ* performed after CO_2 hydrogenation treatment. Briefly, after the activation process under Ar/H_2 or N_2/H_2 atmosphere, the CO_2 hydrogenation reaction was carried out to accumulate surface intermediates and then the H_2-TPR test was performed after cooling down. **Figure 5b** shows the *in-situ* H_2-TPR curves of CM and CMN after CO_2 hydrogenation for 1 h. Interestingly, it is found that the intermediates adsorbed on CMN show much lower hydrogenation temperatures (250 ℃) than those adsorbed on CM (512 ℃), indicating that CMN is with an enhanced hydrogenation ability. Furthermore, to identify the intermediates, *in-situ* diffuse reflectance infrared Fourier transform spectroscopy (DRIFTS) experiments were carried out. No signals of *HCOO or *COOH species are found in the spectra, implying that the *HCOO or *COOH species might be rapidly decomposed to gaseous CO and *OH that could be further hydrogenated to H_2O (**Figure S8**), which is consistent with the previously reported associative mechanisms.[53-55] Moreover, *quasi-in-situ* Raman spectra were also obtained to detect the evolution of the surface structure of catalysts during the reaction. When the surface *OH species are not hydrogenated to H_2O or desorbed in time, it might oxidize the catalyst. As shown in **Figures 5c** and **5d**, a peak at 938

cm^{-1} corresponding to the Mo-O stretching vibration of $CoMoO_4$ is observed in the Raman spectra of fresh CM (CM-fresh) and CMN (CMN-fresh) catalysts due to the passivation treatment.[56-58] For quantification analysis, the areas of Mo-O peak at ~938 cm^{-1} (A_{Mo-O}) and the quartz peak at ~805 cm^{-1} (A_{quartz}) as a reference were integrated. The ratio of A_{Mo-O} to A_{quartz} (A_{Mo-O}/A_{quartz}) can be considered as an indicator to describe the change of the Mo-O bond during the reaction. After the activation process under Ar/H_2 or N_2/H_2 atmosphere, the Mo-O peak disappears for both CM (CM-red) and CMN (CM-red) catalysts due to the removal of the surface oxide layer. After being exposed to the CO_2 hydrogenation atmosphere at 400 ℃ for 1 h, the Mo-O peak appears again in the Raman spectra of CM (CM-rec-1h) and shows a A_{Mo-O}/A_{quartz} of 0.12, but it is not observed for CMN (CMN-rec-1h). Extending the reaction time to 10 h, it is found that the intensity of the Mo-O peak for CM (CM-rec-10h) is further enhanced (0.38 for A_{Mo-O}/A_{quartz}) compared to that of CM-rec-1h and a weak Mo-O peak is also observed in the Raman spectra of CMN (CMN-rec-10h, 0.10 for A_{Mo-O}/A_{quartz}) (**Table S3**). Based on these results, it is suggested that *OH species could oxidize the catalytic surface of both CM and CMN catalysts to $CoMoO_4$ during CO_2 hydrogenation. Compared to CM, CMN is less easy to be oxidized. This means that the O species binding to the surface of CMN is much easier to be removed by H_2, which is consistent with the *in-situ* H_2-TPR results. Therefore, it can be reasonably inferred that the removal of O-containing intermediates is a rate-determining step during CO_2 hydrogenation for CoMo bimetallic catalysts, while the introduced N atoms promote the supply of H species and thus improve the hydrogenation ability of surface Mo-O species, accelerating the redox cycle in CO_2 hydrogenation and ultimately enhancing the RWGS activity. Notably, the accumulation of surface Mo-O species could lead to deactivation

as the formed $CoMoO_4$ is inactive either for CO_2 activation or for H_2 dissociation. Although both CM and CMN catalysts do not show significant deactivation in the 30-h stability test (**Figure 2d**), the N-promoted removal of O species will delay the deactivation during long-term catalytic applications.

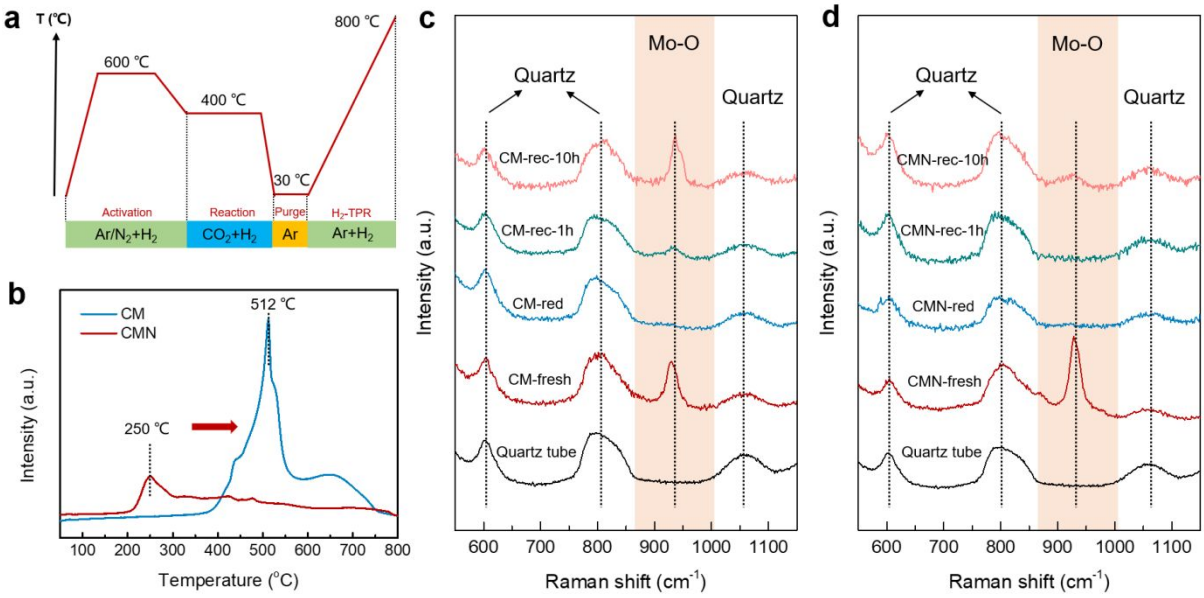

Figure 5 (a) Schematic diagram of H_2-TPR experiment for spent catalysts. (b) H_2-TPR curves of CM and CMN catalysts after CO_2 hydrogenation at 400 ℃ for 1 h. *Quasi-in-situ* Raman spectra of (c) CM and (d) CMN after reduction and reaction with a 325 nm laser.

3.5 Structure-performance relationship determination

So far, it is clear that the introduced N atoms in CoMo bimetallic catalysts increase the sites for increasing the supply of H species during the CO_2 hydrogenation reaction, promoting the removal of surface O intermediates and accelerating the redox cycle in CO_2 hydrogenation. However, according to the electronic structure characterization results of CMN and CM, it is found that the introduced N atoms could accept electrons from Mo and thus lead to the formation of positive charged Mo species (i.e., $Mo^{\delta+}$). Meanwhile, the removal of O

intermediates from the surface of catalysts is essentially a process of H_2-assisted Mo-O bond cleavage. Combining these results, it can be inferred that the introduced N atoms could change Mo-O binding energy, which in turn affects the redox cycle in CO_2 hydrogenation. To further demonstrate this inference, the structure stability of O on the CM and CMN catalysts under a reduction atmosphere was evaluated using density functional theory (DFT) calculations. As shown in **Figures 6a** and **6b**, the H atom is coordinated to two Mo atoms and one Co atom for both CM and CMN catalysts. Meanwhile, the O atom is coordinated to two Mo atoms and one Co atom for CM, while the O atom is coordinated to three Mo atoms for CMN. According to the results of crystal orbital Hamilton populations (COHPs) analysis, H-metal bonds for both CM and CMN show more positive integrated projected COHPs (ICOHPs) values than O-metal bonds, indicating that the migration of H after H_2 dissociation is not the rate-determining step for the O removal process (**Figure S9**, **Figures 6c** and **6d**). For the O-metal coordination, the O-Co bonds also show more positive ICOHPs values than O-Mo bonds, implying that the removal of ligand O on Mo atoms is the key step in the removal of O on CM and CMN catalysts. Furthermore, it is found that the O-Mo bonds on CM (-2.75 eV ~ -2.93 eV) show more negative ICOHPs values than those on CMN catalysts (-2.30 eV ~ -2.33 eV), demonstrating that the introduced N weakens the binding strength of Mo to O. The binding energies (BEs) of H and O on CM and CMN were also calculated, in which the CM and CMN catalysts show a similar BE of H atom (-3.23 eV for CM and -2.99 for CMN) but quite different BEs of O atom (-17.88 eV for CM and -7.00 eV for CMN), which is also consistent with the ICOHP results and quasi-in-situ Raman results. These results indicate that the origin of the N-promoted RWGS activity is enhancing the redox cycle in CO_2 hydrogenation, which is due to that: (1) the introduced N

atoms increase the sites for supplying more H species during CO_2 hydrogenation; (2) the introduction of N atoms induce the formation of $Mo^{\delta+}$ and weaken the binding strength of Mo to O intermediate species.

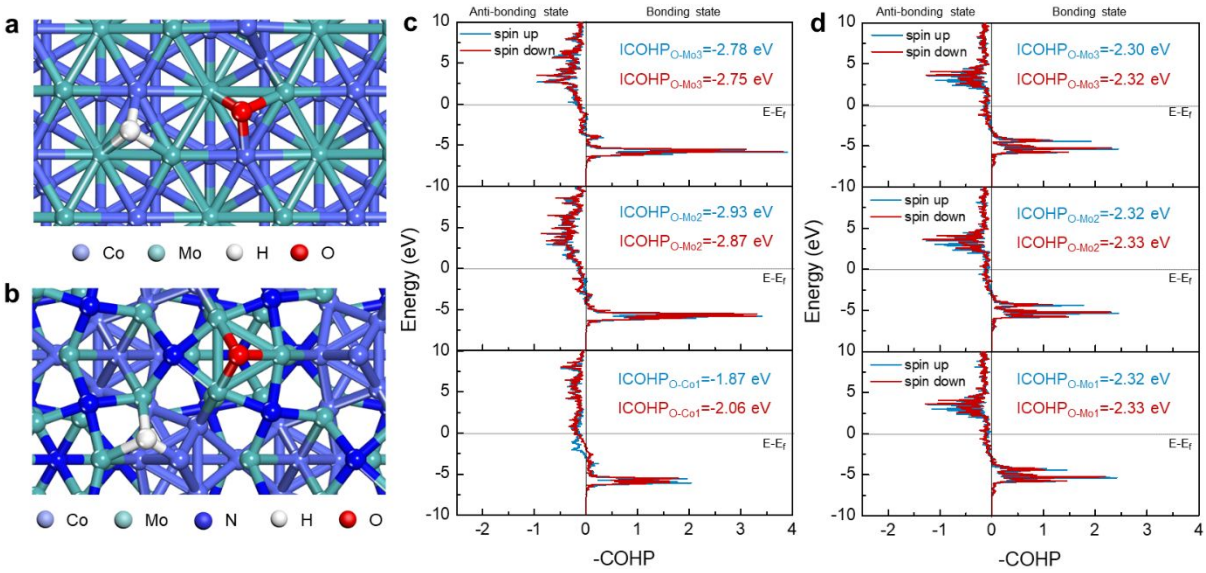

Figure 6 The top view of (a) (001) surface of CM and (b) (111) surface of CMN catalysts for adsorption geometry of H and O. Crystal orbital Hamilton populations (COHPs) analysis for three coordinate bonds of oxygen atoms in (c) CM and (d) CMN.

4. CONCLUSION

In summary, Co_3Mo_3N synthesized by introducing N atoms into CoMo can be employed as a efficient catalyst for the RWGS reaction. The removal of O-containing intermediates is identified as the rate-determining step in the RWGS reaction over Co_3Mo_3N. The introduced N atoms are revealed to play a dual role in enhancing the catalytic performance: (1) forming NH_x species to provide additional sites, increasing the supply of H species to facilitate the CO_2 hydrogenation reaction. (2) accepting electrons from coordinated Mo atoms to form positive charged Mo species ($Mo^{\delta+}$), weakening the binding ability of Mo to key reaction intermediates.

The dual functions improve the hydrogenation ability of surface O-containing intermediates, promote the redox cycle in the hydrogenation of CO_2, and ultimately enhance the RWGS performance. The unraveled origin of the interstitial N atoms promoted RWGS activity for bimetallic nitride provides new insights into the interstitial light elements-promoted catalytic performance relationship.

AUTHOR INFORMATION

Corresponding Author

* binhangyan@tsinghua.edu.cn

Author Contributions

K. Feng, conceived and designed the experiments, carried out the catalyst synthesis and characterization. J. Tian and J. Zhang carried out the DFT calculations. Z. Li carried out the *quasi-in-situ* Raman spectra experiments. Y. Chen carried out the kinetic analysis of temperature-programmed experiments. K. Luo and B. Yang provided resources and support for the DFT calculations. K. Feng and B. Yan wrote the paper. B. Yan provide the financial and equipment support for this work. All authors commented on the final manuscript.

Funding Sources

National Natural Science Foundation of China (NSFC, Grant No. 21978148); High-Performance Parallel Computer supported by the UK Engineering and Physical Sciences Research Council under the project UK Consortium on Mesoscale Engineering Sciences (UKCOMES) (Grant No. EP/R029598/1).

Notes

The authors declare no competing financial interest.

Supporting Information. Schematic diagram for *Ea* evaluation; digital picture of experimental equipment for *quasi-in-situ* Raman spectra measurement; TEM and XRD of CoMo or $CoMoO_4$; CO_2 hydrogenation catalytic performance; *In-situ* DRIFTS for CM and CMN during CO_2 hydrogenation; COHPs analysis for three coordinate bonds of hydrogen atoms in CM and CMN; CO_2 hydrogenation performance of CM and CMN at different temperatures. This information is available free of charge on the ACS Publications website.

ACKNOWLEDGMENTS

This work was supported by the National Natural Science Foundation of China (NSFC, Grant No. 21978148). The authors thank beamline 4B9A at the Beijing Synchrotron Radiation Facility (BSRF) for providing the beam time. The simulations were partly performed on the High-Performance Parallel Computer supported by the UK Engineering and Physical Sciences Research Council under the project UK Consortium on Mesoscale Engineering Sciences (UKCOMES) (Grant No. EP/R029598/1).

REFERENCES

1. Bullock, R. M.; Chen, J. G.; Gagliardi, L.; Chirik, P. J.; Farha, O. K.; Hendon, C. H.; Jones, C. W.; Keith, J. A.; Klosin, J.; Minteer, S. D.; Morris, R. H.; Radosevich, A. T.; Rauchfuss, T. B.; Strotman, N. A.; Vojvodic, A.; Ward, T. R.; Yang, J. Y.; Surendranath, Y., Using nature's blueprint to expand catalysis with Earth-abundant metals. *Science* **2020,** *369* (6505), eabc3183.

2. Nørskov, J. K.; Bligaard, T.; Rossmeisl, J.; Christensen, C. H., Towards the computational design of solid catalysts. *Nat. Chem.* **2009,** *1* (1), 37-46.

3. Studt, F.; Abild-Pedersen, F.; Bligaard, T.; Sorensen, R. Z.; Christensen, C. H.; Norskov, J. K., Identification of non-precious metal alloy catalysts for selective hydrogenation of acetylene. *Science* **2008,** *320* (5881), 1320-1322.

4. Jacobsen, C. J.; Dahl, S.; Clausen, B. S.; Bahn, S.; Logadottir, A.; Norskov, J. K., Catalyst design by interpolation in the periodic table: bimetallic ammonia synthesis catalysts. *J. Am. Chem. Soc.* **2001,** *123* (34), 8404-5.

5. Wang, T.; Cui, X.; Winther, K. T.; Abild-Pedersen, F.; Bligaard, T.; Nørskov, J. K., Theory-aided discovery of metallic catalysts for selective propane dehydrogenation to propylene. *ACS Catal.* **2021**, 6290-6297.
6. Montoya, J. H.; Seitz, L. C.; Chakthranont, P.; Vojvodic, A.; Jaramillo, T. F.; Norskov, J. K., Materials for solar fuels and chemicals. *Nat. Mater.* **2016,** *16* (1), 70-81.
7. Chen, J. G.; Crooks, R. M.; Seefeldt, L. C.; Bren, K. L.; Bullock, R. M.; Darensbourg, M. Y.; Holland, P. L.; Hoffman, B.; Janik, M. J.; Jones, A. K.; Kanatzidis, M. G.; King, P.; Lancaster, K. M.; Lymar, S. V.; Pfromm, P.; Schneider, W. F.; Schrock, R. R., Beyond fossil fuel-driven nitrogen transformations. *Science* **2018,** *360* (6391), eaar6611.
8. Johnson, A. D.; Daley, S. P.; Utz, A. L.; Ceyer, S. T., The chemistry of bulk hydrogen: reaction of hydrogen embedded in nickel with adsorbed CH3. *Science* **1992,** *257* (5067), 223-225.
9. Gao, W.; Guo, J.; Wang, P.; Wang, Q.; Chang, F.; Pei, Q.; Zhang, W.; Liu, L.; Chen, P., Production of ammonia via a chemical looping process based on metal imides as nitrogen carriers. *Nat. Energ.* **2018,** *3* (12), 1067-1075.
10. Wang, P.; Chang, F.; Gao, W.; Guo, J.; Wu, G.; He, T.; Chen, P., Breaking scaling relations to achieve low-temperature ammonia synthesis through LiH-mediated nitrogen transfer and hydrogenation. *Nat. Chem.* **2017,** *9* (1), 64-70.
11. Chen, T.; Ellis, I.; Hooper, T. J. N.; Liberti, E.; Ye, L.; Lo, B. T. W.; O'Leary, C.; Sheader, A. A.; Martinez, G. T.; Jones, L.; Ho, P. L.; Zhao, P.; Cookson, J.; Bishop, P. T.; Chater, P.; Hanna, J. V.; Nellist, P.; Tsang, S. C. E., Interstitial boron atoms in the palladium lattice of an industrial type of nanocatalyst: properties and structural modifications. *J. Am. Chem. Soc.* **2019,** *141* (50), 19616-19624.
12. Ellis, I. T.; Wolf, E. H.; Jones, G.; Lo, B.; Meng-Jung Li, M.; York, A. P.; Edman Tsang, S. C., Lithium and boron as interstitial palladium dopants for catalytic partial hydrogenation of acetylene. *Chem. Commun.* **2017,** *53* (3), 601-604.
13. Chan, C. W.; Mahadi, A. H.; Li, M. M.; Corbos, E. C.; Tang, C.; Jones, G.; Kuo, W. C.; Cookson, J.; Brown, C. M.; Bishop, P. T.; Tsang, S. C., Interstitial modification of palladium nanoparticles with boron atoms as a green catalyst for selective hydrogenation. *Nat. Commun.* **2014,** *5*, 5787.
14. Deng, Y.; Ge, Y.; Xu, M.; Yu, Q.; Xiao, D.; Yao, S.; Ma, D., Molybdenum carbide: controlling the geometric and electronic structure of noble metals for the activation of O-H and C-H bonds. *Acc. Chem. Res.* **2019,** *52* (12), 3372-3383.
15. Marquart, W.; Raseale, S.; Prieto, G.; Zimina, A.; Sarma, B. B.; Grunwaldt, J.-D.; Claeys, M.; Fischer, N., CO2 reduction over Mo2C-based catalysts. *ACS Catal.* **2021,** *11* (3), 1624-1639.
16. Zhang, X.; Liu, Y.; Zhang, M.; Yu, T.; Chen, B.; Xu, Y.; Crocker, M.; Zhu, X.; Zhu, Y.; Wang, R.; Xiao, D.; Bi, M.; Ma, D.; Shi, C., Synergy between β-Mo2C nanorods and non-thermal plasma for selective CO2 reduction to CO. *Chem* **2020,** *6* (12), 3312-3328.
17. Liu, C.; Kang, J.; Huang, Z. Q.; Song, Y. H.; Xiao, Y. S.; Song, J.; He, J. X.; Chang, C. R.; Ge, H. Q.; Wang, Y.; Liu, Z. T.; Liu, Z. W., Gallium nitride catalyzed the direct hydrogenation of carbon dioxide to dimethyl ether as primary product. *Nat. Commun.* **2021,** *12* (1), 2305.
18. Zhao, B.; Sun, M.; Chen, F.; Shi, Y.; Yu, Y.; Li, X.; Zhang, B., Unveiling the activity origin of iron nitride as catalytic material for efficient hydrogenation of CO2 to C2+ hydrocarbons. *Angew. Chem. Int. Ed. Engl.* **2021,** *60* (9), 4496-4500.
19. Wang, L.; Zhang, W.; Zheng, X.; Chen, Y.; Wu, W.; Qiu, J.; Zhao, X.; Zhao, X.; Dai, Y.; Zeng, J., Incorporating nitrogen atoms into cobalt nanosheets as a strategy to boost catalytic activity toward CO2 hydrogenation. *Nat. Energ.* **2017,** *2* (11), 869-876.
20. He, T.; Wang, W.; Shi, F.; Yang, X.; Li, X.; Wu, J.; Yin, Y.; Jin, M., Mastering the surface strain

of platinum catalysts for efficient electrocatalysis. *Nature* **2021,** *598* (7879), 76-81.

21. Tong, Z.; Li, X.; Dong, J.; Gao, R.; Deng, Q.; Wang, J.; Zeng, Z.; Zou, J.-J.; Deng, S., Adsorption configuration-determined selective hydrogenative ring opening and ring rearrangement of furfural over metal phosphate. *ACS Catal.* **2021**, 6406-6415.

22. Li, Z.; Zhang, X.; Liu, J.; Shi, R.; Waterhouse, G. I. N.; Wen, X. D.; Zhang, T., Titania-supported Ni2P/Ni catalysts for selective solar-driven CO hydrogenation. *Adv. Mater.* **2021**, e2103248.

23. Li, S. H.; Qi, M. Y.; Tang, Z. R.; Xu, Y. J., Nanostructured metal phosphides: from controllable synthesis to sustainable catalysis. *Chem. Soc. Rev.* **2021,** *50* (13), 7539-7586.

24. Zhao, B.; Zhai, P.; Wang, P.; Li, J.; Li, T.; Peng, M.; Zhao, M.; Hu, G.; Yang, Y.; Li, Y.-W.; Zhang, Q.; Fan, W.; Ma, D., Direct transformation of syngas to aromatics over Na-Zn-Fe5C2 and hierarchical HZSM-5 tandem catalysts. *Chem* **2017,** *3* (2), 323-333.

25. Gao, W.; Gao, R.; Zhao, Y.; Peng, M.; Song, C.; Li, M.; Li, S.; Liu, J.; Li, W.; Deng, Y.; Zhang, M.; Xie, J.; Hu, G.; Zhang, Z.; Long, R.; Wen, X.-D.; Ma, D., Photo-driven syngas conversion to lower olefins over oxygen-decorated Fe5C2 catalyst. *Chem* **2018,** *4* (12), 2917-2928.

26. Zhang, X.; Zhu, X.; Lin, L.; Yao, S.; Zhang, M.; Liu, X.; Wang, X.; Li, Y.-W.; Shi, C.; Ma, D., Highly dispersed copper over β-Mo2C as an efficient and stable catalyst for the reverse water gas shift (RWGS) reaction. *ACS Catal.* **2016,** *7* (1), 912-918.

27. Song, C. Q.; Liu, X.; Xu, M.; Masi, D.; Wang, Y. G.; Deng, Y. C.; Zhang, M. T.; Qin, X. T.; Feng, K.; Yan, J.; Leng, J.; Wang, Z. H.; Xu, Y.; Yan, B. H.; Jin, S. Y.; Xu, D. S.; Yin, Z.; Xiao, D. Q.; Ma, D., Photothermal conversion of CO2 with tunable selectivity using Fe-based catalysts: from oxide to carbide. *ACS Catal.* **2020,** *10* (18), 10364-10374.

28. Wang, Y.; Liu, B.; Lan, X.; Wang, T., Subsurface carbon as a selectivity promotor to enhance catalytic performance in acetylene semihydrogenation. *ACS Catal.* **2021**, 10257-10266.

29. Niu, Y.; Huang, X.; Wang, Y.; Xu, M.; Chen, J.; Xu, S.; Willinger, M. G.; Zhang, W.; Wei, M.; Zhang, B., Manipulating interstitial carbon atoms in the nickel octahedral site for highly efficient hydrogenation of alkyne. *Nat. Commun.* **2020,** *11* (1), 3324.

30. Yao, S.; Zhang, X.; Zhou, W.; Gao, R.; Xu, W.; Ye, Y.; Lin, L.; Wen, X.; Liu, P.; Chen, B.; Crumlin, E.; Guo, J.; Zuo, Z.; Li, W.; Xie, J.; Lu, L.; Kiely, C. J.; Gu, L.; Shi, C.; Rodriguez, J. A.; Ma, D., Atomic-layered Au clusters on alpha-MoC as catalysts for the low-temperature water-gas shift reaction. *Science* **2017,** *357* (6349), 389-393.

31. Zhang, X.; Zhang, M.; Deng, Y.; Xu, M.; Artiglia, L.; Wen, W.; Gao, R.; Chen, B.; Yao, S.; Zhang, X.; Peng, M.; Yan, J.; Li, A.; Jiang, Z.; Gao, X.; Cao, S.; Yang, C.; Kropf, A. J.; Shi, J.; Xie, J.; Bi, M.; van Bokhoven, J. A.; Li, Y. W.; Wen, X.; Flytzani-Stephanopoulos, M.; Shi, C.; Zhou, W.; Ma, D., A stable low-temperature H2-production catalyst by crowding Pt on alpha-MoC. *Nature* **2021,** *589* (7842), 396-401.

32. Lin, L.; Zhou, W.; Gao, R.; Yao, S.; Zhang, X.; Xu, W.; Zheng, S.; Jiang, Z.; Yu, Q.; Li, Y. W.; Shi, C.; Wen, X. D.; Ma, D., Low-temperature hydrogen production from water and methanol using Pt/alpha-MoC catalysts. *Nature* **2017,** *544* (7648), 80-83.

33. Lin, L.; Yu, Q.; Peng, M.; Li, A.; Yao, S.; Tian, S.; Liu, X.; Li, A.; Jiang, Z.; Gao, R.; Han, X.; Li, Y. W.; Wen, X. D.; Zhou, W.; Ma, D., Atomically dispersed Ni/alpha-MoC catalyst for hydrogen production from methanol/water. *J. Am. Chem. Soc.* **2021,** *143* (1), 309-317.

34. Ge, Y.; Qin, X.; Li, A.; Deng, Y.; Lin, L.; Zhang, M.; Yu, Q.; Li, S.; Peng, M.; Xu, Y.; Zhao, X.; Xu, M.; Zhou, W.; Yao, S.; Ma, D., Maximizing the synergistic effect of CoNi catalyst on alpha-MoC for robust hydrogen production. *J. Am. Chem. Soc.* **2021,** *143* (2), 628-633.

35. Feng, K.; Wang, Y.; Guo, M.; Zhang, J.; Li, Z.; Deng, T.; Zhang, Z.; Yan, B., In-situ/operando techniques to identify active sites for thermochemical conversion of CO2 over heterogeneous catalysts. *J. Energ. Chem.* **2021,** *62*, 153-171.

36. Kim, K. Y.; Lee, J. H.; Lee, H.; Noh, W. Y.; Kim, E. H.; Ra, E. C.; Kim, S. K.; An, K.; Lee, J. S., Layered double hydroxide-derived intermetallic Ni3GaC0.25 catalysts for dry reforming of methane. *ACS Catal.* **2021**, 11091-11102.

37. Porosoff, M. D.; Yan, B.; Chen, J. G., Catalytic reduction of CO2 by H2 for synthesis of CO, methanol and hydrocarbons: challenges and opportunities. *Energ. Environ. Sci.* **2016,** *9* (1), 62-73.

38. Wang, Y.; Winter, L. R.; Chen, J. G.; Yan, B., CO2 hydrogenation over heterogeneous catalysts at atmospheric pressure: from electronic properties to product selectivity. *Green Chem.* **2021,** *23* (1), 249-267.

39. Kattel, S.; Liu, P.; Chen, J. G., Tuning selectivity of CO2 hydrogenation reactions at the metal/oxide interface. *J. Am. Chem. Soc.* **2017,** *139* (29), 9739-9754.

40. Feng, K.; Wang, S.; Zhang, D.; Wang, L.; Yu, Y.; Feng, K.; Li, Z.; Zhu, Z.; Li, C.; Cai, M.; Wu, Z.; Kong, N.; Yan, B.; Zhong, J.; Zhang, X.; Ozin, G. A.; He, L., Cobalt Plasmonic Superstructures Enable Almost 100% Broadband Photon Efficient CO2 Photocatalysis. *Adv. Mater.* **2020,** *32* (24), e2000014.

41. Xu, Y. F.; Duchesne, P. N.; Wang, L.; Tavasoli, A.; Jelle, A. A.; Xia, M.; Liao, J. F.; Kuang, D. B.; Ozin, G. A., High-performance light-driven heterogeneous CO2 catalysis with near-unity selectivity on metal phosphides. *Nat. Commun.* **2020,** *11* (1), 5149.

42. Lou, D. Y.; Zhu, Z. J.; Xu, Y. F.; Li, C. R.; Feng, K.; Zhang, D. K.; Lv, K. X.; Wu, Z. Y.; Zhang, C. C.; Ozin, G. A.; He, L.; Zhang, X. H., A core-shell catalyst design boosts the performance of photothermal reverse water gas shift catalysis. *Sci. China Mater.* **2021,** *64* (9), 2212-2220.

43. Zhou, H.; Chen, Z.; Kountoupi, E.; Tsoukalou, A.; Abdala, P. M.; Florian, P.; Fedorov, A.; Muller, C. R., Two-dimensional molybdenum carbide 2D-Mo2C as a superior catalyst for CO2 hydrogenation. *Nat. Commun.* **2021,** *12* (1), 5510.

44. Xie, Z.; Yan, B.; Zhang, L.; Chen, J. G., Comparison of methodologies of activation barrier measurements for reactions with deactivation. *Ind. Eng. Chem. Res.* **2017,** *56* (5), 1360-1364.

45. Ge, R.; Huo, J.; Li, Y.; Liao, T.; Zhang, J.; Zhu, M.; Ahamad, T.; Li, S.; Liu, H.; Feng, L.; Li, W., Electrocatalyst nanoarchitectonics with molybdenum-cobalt bimetallic alloy encapsulated in nitrogen-doped carbon for water splitting reaction. *J. Alloys Compd.* **2022,** *904*, 164084.

46. Zeinalipour-Yazdi, C. D.; Hargreaves, J. S. J.; Catlow, C. R. A., Nitrogen activation in a Mars-van Krevelen mechanism for ammonia synthesis on Co3Mo3N. *J. Phys. Chem. C* **2015,** *119* (51), 28368-28376.

47. Zeinalipour-Yazdi, C. D.; Hargreaves, J. S. J.; Catlow, C. R. A., DFT-D3 study of molecular N2 and H2 activation on Co3Mo3N surfaces. *J. Phys. Chem. C* **2016,** *120* (38), 21390-21398.

48. Kojima, R.; Aika, K.-i., Cobalt molybdenum bimetallic nitride catalysts for ammonia synthesis Part 1. Preparation and characterization. *Appl. Catal., A* **2001,** *215* (1-2), 149-160.

49. Adamski, P.; Moszynski, D.; Komorowska, A.; Nadziejko, M.; Sarnecki, A.; Albrecht, A., Ammonolysis of cobalt molybdenum oxides - in situ XRD study. *Inorg. Chem.* **2018,** *57* (16), 9844-9850.

50. Yao, S.; Lin, L.; Liao, W.; Rui, N.; Li, N.; Liu, Z.; Cen, J.; Zhang, F.; Li, X.; Song, L.; Betancourt De Leon, L.; Su, D.; Senanayake, S. D.; Liu, P.; Ma, D.; Chen, J. G.; Rodriguez, J. A., Exploring metal-support interactions to immobilize subnanometer Co clusters on γ-Mo2N: a highly selective and stable catalyst for CO2 activation. *ACS Catal.* **2019,** *9* (10), 9087-9097.

51. Vogt, C.; Monai, M.; Sterk, E. B.; Palle, J.; Melcherts, A. E. M.; Zijlstra, B.; Groeneveld, E.; Berben, P. H.; Boereboom, J. M.; Hensen, E. J. M.; Meirer, F.; Filot, I. A. W.; Weckhuysen, B. M., Understanding carbon dioxide activation and carbon-carbon coupling over nickel. *Nat. Commun.* **2019,** *10* (1),

5330.

52. Feng, K.; Tian, J.; Guo, M.; Wang, Y.; Wang, S.; Wu, Z.; Zhang, J.; He, L.; Yan, B., Experimentally unveiling the origin of tunable selectivity for CO2 hydrogenation over Ni-based catalysts. *Appl. Catal., B* **2021,** *292*, 120191.

53. Gu, M.; Dai, S.; Qiu, R.; Ford, M. E.; Cao, C.; Wachs, I. E.; Zhu, M., Structure-activity relationships of copper- and potassium-modified iron oxide catalysts during reverse water-gas shift reaction. *ACS Catal.* **2021,** *11*, 12609-12619.

54. Bobadilla, L. F.; Santos, J. L.; Ivanova, S.; Odriozola, J. A.; Urakawa, A., Unravelling the role of oxygen vacancies in the mechanism of the reverse water-gas shift reaction by operando DRIFTS and ultraviolet-visible spectroscopy. *ACS Catal.* **2018,** *8* (8), 7455-7467.

55. Zhu, M.; Chen, J.; Shen, L.; Ford, M. E.; Gao, J.; Xu, J.; Wachs, I. E.; Han, Y.-F., Probing the surface of promoted CuO-Cr2O3-Fe2O3 catalysts during CO2 activation. *Appl. Catal., B* **2020,** *271*, 118943.

56. Mestl, G.; Srinivasan, T. K. K., Raman spectroscopy of monolayer-type catalysts: supported molybdenum oxides. *Catal. Rev.* **1998,** *40* (4), 451-570.

57. Jeziorowski, H.; Knoezinger, H.; Grange, P.; Gajardo, P., Raman spectra of cobalt molybdenum oxide supported on silica. *J. Phys. Chem.* **1980,** *84* (14), 1825-1829.

58. Herrera, J. E.; Resasco, D. E., Loss of single-walled carbon nanotubes selectivity by disruption of the Co-Mo interaction in the catalyst. *J. Catal.* **2004,** *221* (2), 354-364.

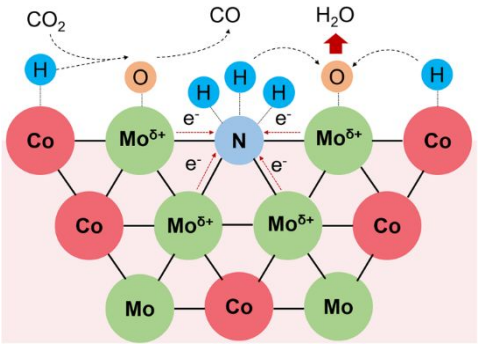

For Table of Contents Only